GPS Solutions (2022) 26:22
https://doi.org/10.1007/s10291-021-01207-x

ORIGINAL ARTICLE

Tidal measurements in the Gulf of Mexico: intercomparison of coastal tide gauge, insular GNSS reflectometry and SAR altimetry

Carlos A. Martinez-Felix[1] · G. Esteban Vazquez-Becerra[1] · Felipe Geremia-Nievinski[2] · Jesus R. Millan-Almaraz[3] · Cuauhtemoc Franco-Ochoa[4] · Angela Melgarejo-Morales[1] · J. Ramon Gaxiola-Camacho[4]

Received: 10 March 2021 / Accepted: 23 November 2021

Abstract
Sea level can be monitored using conventional tide gauges, ground-based Global Navigation Satellite System Reflectometry (GNSS-R), and synthetic aperture radar (SAR) satellite altimetry. Each technique has its advantages and disadvantages, so an intercomparison is a good exercise for cross-validation. We analyze the reliability of a standard geodetic-grade GNSS receiver and antenna and two Sentinel-3A SAR products to measure sea level variations in the Gulf of Mexico. We considered a one-year period over a 120 km wide region between an island and mainland, composed of reefs and shallow waters. First, signal-to-noise ratio (SNR) observations from a GNSS station (CN26) on the island were analyzed. Second, high-resolution SAR altimetry data (20 Hz) of the Sentinel-3A satellite were acquired based on two processors, SARvatore and Peachi. The above results were compared to a conventional tide gauge located on the mainland at the shoreline of Progreso, Yucatan. The GNSS-R relative sea level had a correlation of 0.84 and root-mean-square error (RMSE) of 7.8 cm with the tide gauge, while SAR altimetry products had a correlation and RMSE of 0.86 12.4 cm for SARvatore and 0.85, 12.8 cm for Peachi. Furthermore, correlation and RMS between GNSS-R and SAR were found to be 0.94, 8.6 cm for SARvatore and 0.95, 7.2 cm for Peachi. Meanwhile, SARvatore and Peachi achieved an internal correlation of 0.92 and RMSE of 8.9 cm. Moreover, scale variations caused by the differences in the tidal range were quantified by linear regression slope with respect to the tide gauge, which amounted to 0.554, 0.843 and 0.814, respectively, for GNSS-R, SARvatore and Peachi. Finally, derived daily GNSS-R observations in conjunction with SAR altimetry were coherent with respect to the reference tide gauge indicating that GNSS-R can operate as an auxiliary validation instrument for SAR altimetry coastal measurements at ungauged locations.

Keywords GNSS-R · Reflectometry · Multipath · SNR · Sea level · Coastal altimetry

✉ G. Esteban Vazquez-Becerra
gvazquez@uas.edu.mx

Carlos A. Martinez-Felix
carlosmartinez@uas.edu.mx

Felipe Geremia-Nievinski
felipe.nievinski@ufrgs.br

Jesus R. Millan-Almaraz
jr.millan.almaraz@gmail.com

Cuauhtemoc Franco-Ochoa
cfrancoo@uas.edu.mx

Angela Melgarejo-Morales
angelamelgarejo@uas.edu.mx

J. Ramon Gaxiola-Camacho
jrgaxiola@uas.edu.mx

[1] Department of Earth and Space Science, Autonomous University of Sinaloa, 80040 Culiacan, Sinaloa, Mexico

[2] Department of Geodesy, Institute of Geosciences, Federal University of Rio Grande Do Sul, Porto Alegre, RS 90650-001, Brazil

[3] Department of Physics-Mathematics Science, Autonomous University of Sinaloa, 80040 Culiacan, Sinaloa, Mexico

[4] Department of Civil Engineering, Autonomous University of Sinaloa, 80040 Culiacan, Sinaloa, Mexico

Published online: 07 December 2021

Introduction

Severe hurricanes, droughts, and thunderstorms are one of the consequences and hazards of climate change. Particularly, the increase in temperatures in the past decades compared to centuries ago has caused polar ice caps and continental glaciers to melt rapidly, causing a considerable increase in freshwater input to the oceans. This increased global mean sea level, affecting coastal populations and the global economy.

In the early 1990s, Martin-Neira (1993) proposed a new method to determine and monitor sea level by analyzing the reflections of the Global Positioning System (GPS) radio waves reflected on the sea surface. A few years later, new methodologies were developed using GPS and similar Global Navigation Satellite System reflectometry (GNSS-R) through the analysis of phase delay (Soulat et al. 2004). In particular, fruitful has been the use of signal-to-noise ratio (SNR) observations, pioneered by Anderson (2000), later demonstrated using geodetic-grade GPS/GNSS receivers (Larson et al. 2013). Since then, many existing GNSS stations have been demonstrated for GNSS-R applied to coastal sea level sensing (Geremia-Nievinski et al. 2020a, b).

On the other hand, satellite radar altimetry remains the main instrumentation to measure sea level in the open ocean, using data collected for multiple decades from different missions such as TOPEX and Jason-1/2/3 (Cipollini et al. 2017). However, in the coastal zones, land interferes and contaminates the sensing footprint of spaceborne altimeters, making its validation ambiguous when using coastal tide gauges (Aldarias et al. 2020). For this purpose, several efforts have been made to improve altimetric retrievals by retracking the reflection waveforms, since they start to deviate from a Brown-based waveform when the satellite approaches the coast (Lumban-Gaol et al. 2018). Moreover, new altimetry missions and sensors have improved resolution, especially the Synthetic Aperture Radar (SAR) altimetry mode (Birgiel et al. 2019). Its 20 Hz derived products are used for monitoring sea levels in the coastal zone with better accuracy (Dinardo et al. 2018).

The above-mentioned developments represent an alternative in the remote sensing of sea level. However, they are still not better in accuracy and precision than a conventional tide gauge, whose accuracy ranges from 2 to 12 cm depending on different climatic and temporal factors (Lumban-Gaol et al. 2018). The main drawback of tide gauges is their limited number and coverage area. GNSS-R studies reported RMS errors in a range of 2.1 cm and 25.1 cm, with most of the cases reporting an error of 10 cm. The height precision of GNSS-R is dependent on the time resolution involved in the comparison to tide gauges (e.g., hourly vs daily). Other circumstances also must be considered, such as the GNSS-R technique used for the reflector height retrieval, the distance between the GNSS station and the tide gauge, GNSS site obstruction conditions, and differences in the sampling rates between the GNSS, tide gauge and SAR, among others.

We investigate a cross-validation between SAR altimetry and GNSS-R on an island using a coastal tide gauge, which is unprecedented in the literature. Accordingly, GNSS stations installed worldwide in coastal and insular regions could be used for SAR altimetry validation. We analyzed the two sea-level remote sensing techniques above (GNSS-R and SAR altimetry) for one year in the Gulf of Mexico. First, we demonstrated GNSS-R in a coastal geodetic station under challenging conditions like nearby shallow waters and restricted azimuthal visibility. When selecting the study area, a relevant consideration was the existence of a nearby tide gauge for further validation. Additionally, one year of SAR altimetry data was acquired within 10 km from the GNSS station. Hence, the principal aim of this study was to exploit this opportunity and illustrate this proposition with a particular case of study as well as evaluate and understand the limitations of the two techniques in sea level retrievals. Recently, Holden and Larson (2021) demonstrated GNSS-R for satellite altimetry calibration/validation, for a station located in the interior of a lake, which is a more favorable environment than the island here investigated.

Site description

Isla Pérez is a small island (185 m by 750 m) in the Alacranes reef, declared a national park of Mexico. The GNSS station CN26 is located at the geographical coordinates 22° 22′ 58.80″ N, – 89° 40′ 56.58″ W with an ellipsoidal elevation of – 10.067 m (Fig. 1 right panel). On the ground, it is placed approximately 10 m from the Mean High Water Springs (MHWS) and 15 m from the Mean Low Water Springs (MLWS) (see Fig. 2). The astronomical tide is of mixed type: diurnal tides predominate, while semidiurnal tides occur during neap tides; during neap and spring tides, the tide range varies between 0.1 m and 0.8 m, respectively (Cuevas-Jimenez and Euan-Avila 2009).

The azimuth quadrant between 50° and 130° (in clockwise order), in conjunction with elevation angles from 0 to 20°, can be used to receive GNSS radio-wave reflections from the sea due to geographical constraints (see Fig. 2). The GNSS station is equipped with a Trimble NETR9 geodetic receiver and a choke ring antenna (code TRM59800.00), recording data with a 15 s sampling interval. The station is operated and maintained by UNAVCO as part of the

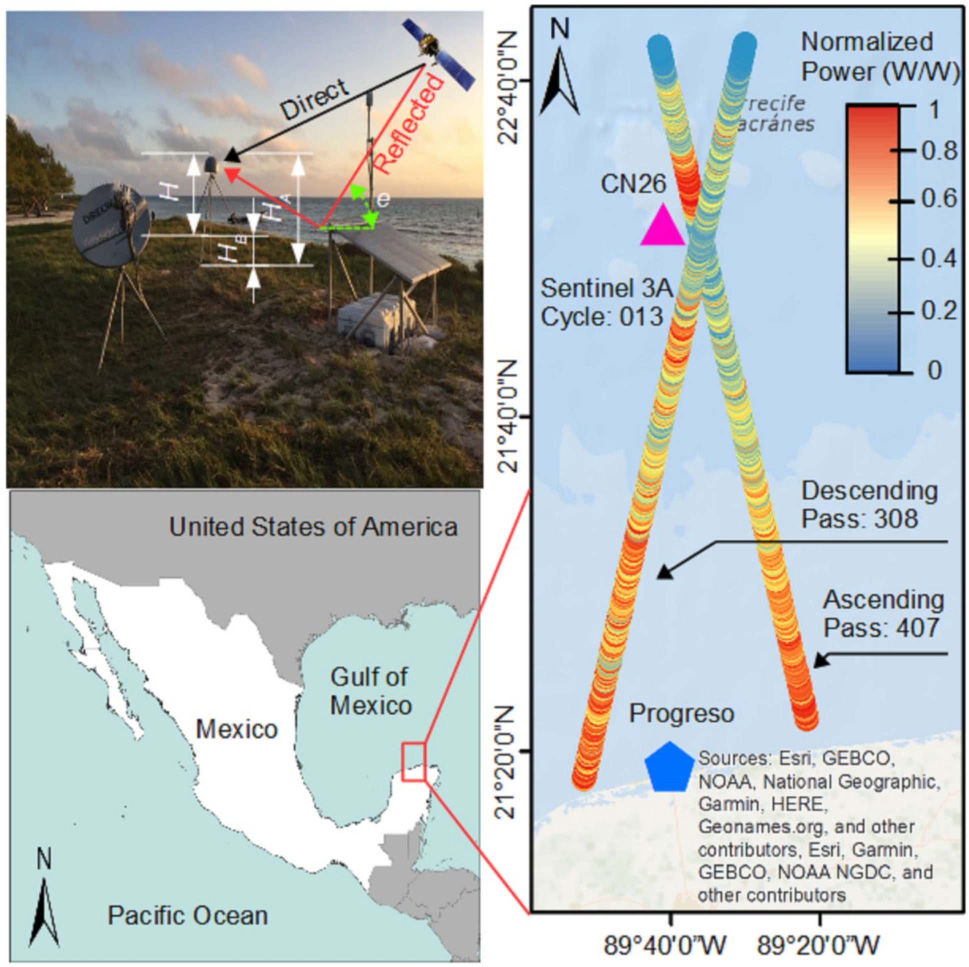

Fig. 1 Study area of the present research. Location of the GNSS station CN26 and tide gauge Progreso (right panel). Installation and instrumentation of GNSS site (top-left panel). In the present analysis, $H_A \equiv 1.8$ m would represent the nominal height of the antenna above mean sea level and H_B would be the unknown tidal variation plus smaller errors in the a priori H_A

COCONet network (Braun et al. 2012). The availability of raw data defined the study time period (year 2017).

The nearest tide gauge station (Progreso) is located approximately 120 km away from the island, on the mainland. It is a radar-type tide gauge with a 1-min sampling interval operated by the National Tide Service of Mexico in conjunction with the Caribbean Tsunami Warning Program administered by the U.S. National Oceanic and Atmospheric Administration.

GNSS-R processing strategy

When establishing a GNSS-R site for sea level sensing, a considerable portion of the sensing zone must be on the water, ensuring that the radio waves from the reflecting surface come from the sea (Geremia-Nievinski and Hobiger 2019). This sensing is formulated in terms of first Fresnel zones (FFZ, see Fig. 2), whose geometry characteristics are described in Larson et al. (2017). FFZ in Fig. 2 corresponds to the L2 C frequency ($\lambda = 24.45$cm) at elevation angles (e) of 5°, 10°, 15° and 20° and an azimuth range of 50° to 130°; a nominal reflector height of $H_A \equiv 1.8$m was obtained by visual inspection of site photographs, corresponding to the antenna height above the mean sea level, excluding tidal variations. However, since the FFZ from high elevation angles might cover both sea and land surface, it is necessary to quantify the land cover effect (see Table 1). It is worth mentioning that for each satellite elevation angle there is a different FFZ and reflection point. From Table 1, FFZ from high elevation angles (> 10°) is partially on land coverage. On the other hand, FFZ semi-major axis length at 5° covers a higher percentage of water.

The main observation used in ground-based GNSS-R is the signal-to-noise ratio (SNR), which is routinely recorded by the receivers and represents the ratio between the signal power and the noise power density (Bilich et al. 2007). Under multipath reception conditions, SNR will record an interference pattern whose oscillations directly relate to the phase difference between reflected and direct waves (Axelrad et al. 2005).

In order to retrieve sea level, we applied a forward and inverse model for SNR observations (Tabibi et al. 2020). It was first proposed by Nievinski and Larson (2014a) and

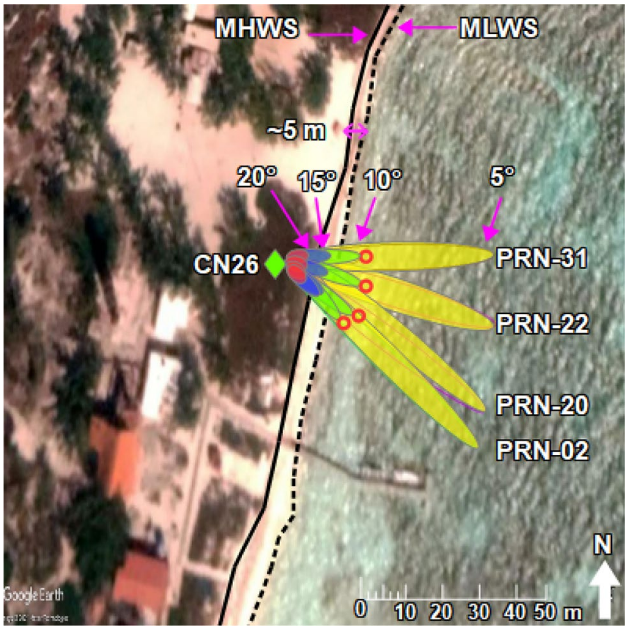

Fig. 2 Illustration of GNSS-R first Fresnel zones (FFZ) for a nominal GNSS antenna height of $H_A \equiv 1.8$ m and four representative satellite tracks (PRN 02, 20, 22, 31) at fixed elevation angles (5°, 10°, 15°, 20°); red rings depict average specular points of each track

Table 1 Distance to specular points relative to the antenna (D), distance to first Fresnel zone (FFZ) center relative to the antenna (R), FFZ semi-major axis length (a) and distance to the FFZ near end ($R_{min} = R - a$)

Satellite elevation	Specular point	First fresnel zone (FFZ)		
e(°)	D(m)	R(m)	a(m)	R_{min}(m)
5	20.6	36.6	30.4	6.2
10	10.2	14.2	10.0	4.2
15	6.7	8.5	5.3	3.2
20	4.9	5.9	3.5	2.4

validated to estimate snow depth around GNSS stations in North America (Nievinski and Larson 2014b) and later in Europe (Tabibi et al. 2017). In this model, SNR observations are represented as $\mathrm{SNR} = P_s/P_n$ the ratio of signal power P_s and noise power P_n. In turn, the signal power is a function of direct P_d and reflected P_r powers as well as direct ϕ_d and reflected ϕ_r phases, as follows. The SNR model can be decomposed into a trend plus detrended interference fringes in the form $\mathrm{SNR} = \mathrm{tSNR} + \mathrm{dSNR}$, where each term can be formulated as:

$$\mathrm{tSNR} = \left(P_d + P_r\right)P_n^{-1} = \left(1 + P_i\right)P_d P_n^{-1} \tag{1}$$

$$\mathrm{dSNR} = 2\sqrt{P_d}\sqrt{P_r}P_n^{-1}\cos\phi_i = 2\sqrt{P_i}P_d P_n^{-1}\cos\phi_i \tag{2}$$

The interferometric phase is defined as $\phi_i = \phi_r - \phi_d$ and the interferometric power as $P_i = P_r/P_d$. The interferometric phase can be approximated as $\phi_i \approx 2\pi\lambda^{-1} \cdot 2H\sin e$ in terms of the reflector height H above a planar and leveled reflecting surface and λ is the carrier wavelength. The quantities above are derived from a physically based forward simulation of radio wave reflection, based on the surface material composition and the antenna gain pattern, among other parameters. Any imperfections in these physical parameters are corrected for using empirical biases that augment the forward model as follows (Nievinski and Larson 2014a):

$$\mathrm{SNR} = \left(1 + P_i' + 2\sqrt{P_i'}\cos\phi_i'\right)P_d'/P_n \tag{3}$$

The augmented quantities read: $P_i' = P_i/B^2$, $\phi_i' = \phi_i - \phi_B$, and $P_d' = P_d/K$. The factor $K = 10^{K_{dB}/10}$ is a real-valued noise power bias that follows from $K_{dB} = K_{dB}^{(0)} + K_{dB}^{(0)}\sin e + K_{dB}^{(2)}\sin^2 e + \ldots$ expressed in decibels units and expanded as a polynomial function of sine of elevation angle. In addition, it is necessary to handle a complex-valued interferometric bias $B = |B|\exp\left(\sqrt{-1}\phi_B\right)$ that can also be expanded into polynomial form for the reflection power bias B_{dB} in decibels and for the reflection phase bias ϕ_B. The linear polynomial coefficient of phase bias $\phi_B^{(1)}$ is the main unknown of interest as it can be transformed into an equivalent reflector height bias in the form $H_B = \phi_B^{(1)}\lambda/4\pi$. Following this concept, the total reflector height can be retrieved as the difference between an a priori first-guess value H_A and the a-posteriori bias estimate H_B as $H = H_A - H_B$. The inverse model fits the theoretical model above to field measurements employing a nonlinear least-squares procedure. This estimated height corresponds to the vertical distance from the antenna phase center to the reflector surface, which is the seawater in this study.

The SNR pattern is in function of the multipath interference and the antenna gain, where the reflection-minus-direct phase corresponds to the sinusoid argument which is driven by the reflection propagation delay. The latter has units of meter and is equivalent to $2H\sin e$, where H is the unknown sea level relative to the antenna and e is the satellite elevation angle (Geremia-Nievinski et al. 2020a). Based on the FFZ described in Fig. 2, an azimuth and elevation angle range mask can be defined to isolate the SNR observations coming only from the sea. Commonly, the optimal SNR observations have a damped sinusoid form, with approximately 6 to 7 peaks for a 2 m antenna that are decreasing in amplitude as the elevation angle increases (Fig. 3 top-left and top-right). Furthermore, when the reflection interacts with a heterogeneous medium with distinct physical composition, the sinusoid begins to deteriorate, presenting secondary reflections and atypical or vanishing interference fringes (see Fig. 3 bottom-left and bottom-right). Therefore, we can select and

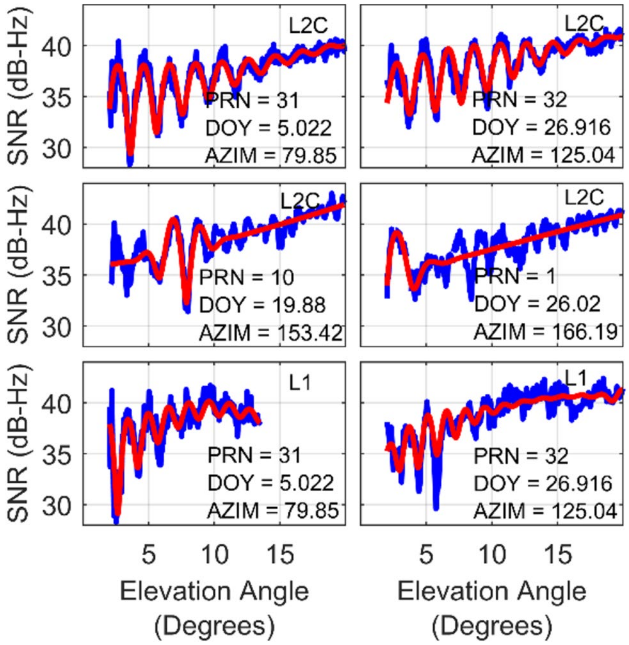

Fig. 3 Examples of SNR observations, measured (blue line) and modeled (red line) SNR signals

improve the best azimuth mask based on the optimal-fit SNR observations to avoid undue noise in the height retrievals.

We used 8034 height retrievals from 19 GPS satellite tracks carrying the L2C modulation (see Fig. 2) due to its improved precision for GNSS reflections studies, compared to the L1 signal (Larson et al. 2017). It was not feasible to apply a height-rate correction using the GNSS-R sea level retrievals (Larson et al. 2013), because there were few usable rising and setting tracks. Considering that the tidal range at this site is less than 80 cm, the effect of height-rate correction should be negligible (Löfgren et al. 2014). Unfortunately, for this specific GPS site, there were no other GNSS observations recorded by the receiver, such as GLONASS, that could otherwise be used to improve the temporal resolution of the GNSS-R time series.

SAR altimetry processing

The Sentinel-3A satellite altimetry mission was selected due to the time span and the SAR-mode data availability, launched in February 2016. The payload instrument (SRAL) provides an enhanced along-track (azimuth) resolution of the order of 300 m. The satellite ascending and descending tracks for cycle 13 and pass 308 and 407 can be visualized in Fig. 1 (right panel). In the latter, the normalization was done by computing the maximum peak power amplitude ratio of the SAR waveforms from the tracks in order to distinguish the noise effect over shallow waters and open sea.

We processed the SRAL level-1A data product to obtain the level-1B radar echogram and level-2 geophysical products through the SAR Versatile Altimetric Toolkit for Ocean Research and Exploitation (SARvatore) software. Both altimetry data and processing tools can be freely accessed online, at https://gpod.eo.esa.int/ (Dinardo et al. 2018). The processing chain is divided into two main phases. The first phase is a set of seven processing stages whose main purpose is to obtain the radar echogram (L1-B) from the raw altimetry data (L1-A). The second phase consists of eight stages and takes as input the data resulting from the previous step (L1-B) in order to obtain L2 geophysical products based on the SAMOSA + retracking algorithm (Ray et al. 2015). Readers are referred to Dinardo (2013) for further details on the processing stages. Later, we applied a post-processing step to SAR observations to restore the effects of the tide and consider the sea state bias (SSB) that were removed from the initial solution. More specifically, we have added the ocean equilibrium tide correction from the FES2014b and subtracted the SSB solution from Jason 2 CLS, both included in the SAR datasets. This was necessary to make SAR results more comparable to the tide gauge and GNSS-R.

In addition, since February 2020, the Archiving, Validation and Interpretation of Satellite Oceanographic data (AVISO +), has released a Sentinel-3 data product based on the coastal enhanced Prototype for Expertise on AltiKa for Coastal, Hydrology and Ice (Peachi). It uses a dedicated retracking algorithm that consists of classifying the different echo shapes retrieved up to 13 different classes through a neural network algorithm to retrieve reliable geophysical parameters; readers are referred to Valladeau et al. (2015), for extensive details on the retracking procedure. This new Sentinel-3 product data is an opportunity to expand the quantity of satellite altimetry measurements that can lead in a denser time series.

Therefore, to build a suitable satellite altimetry time series to compare with other techniques for a one-year time span, we located the SAR observation closer to the tide gauge on the mainland and closer to the GNSS station on the island. It is worth mentioning that SAR altimetry retrievals present a temporal spacing of two observations set per month with four days between each dataset pair. For the whole year 2017, Sentinel-3A cycles 13 to 26 were used and 51 datasets, composed of 27 descending and 24 ascending tracks, were downloaded from the Grid-Processing On-Demand (GPOD) database, maintained by ESA. Additionally, 26 datasets composed of 14 descending and 12 ascending tracks were downloaded from the AVISO + database.

Sea level results and discussion

The tide gauge (TG), GNSS-R and the SAR altimeter employ different types of vertical datum. The TG measurements originally represent the distance between the sensor internal origin and sea level, although an offset may be applied to connect the TG to a benchmark network. GNSS-R retrievals correspond to the distance between the antenna phase center and the reflective surface, which may be further connected to the earth's ellipsoid via GNSS positioning if necessary. Therefore, in order to compare the sea level variations between the proposed instruments, it was necessary to shift the vertical origin in TG and the GNSS-R sea levels measurements. This was done by subtracting the mean sea level from time series of each instrument so as to form relative sea levels. In addition to this step, the tide gauge observations were interpolated to meet the sampling of the GNSS-R observations.

In Fig. 4, it is shown one year of TG sea level variations against 229 days of GNSS-R retrievals and 154 Sentinel-3A SAR-mode observations extracted from the two products. The gaps presented in the GNSS-R time series are a consequence of the missing data due to issues with the instrumentation as well as the azimuth and elevation angle masks imposed in the processing step.

Additionally, since the geographical distance between TG and GNSS receiver is significant (120 km), we have used the FES2014b tidal model to check the tide variations across the two locations. With the aim of evaluating the correlation and precision of the GNSS-R tide gauge and SAR altimetry sea level retrievals, a scatterplot is presented (see Fig. 5). Linear regression was applied to account for scale differences between the techniques. The regression slope values given in Table 2 result from the different tidal ranges experienced across the 120-km distance between GNSS-R, TG and the SAR altimetry and instrumental issues.

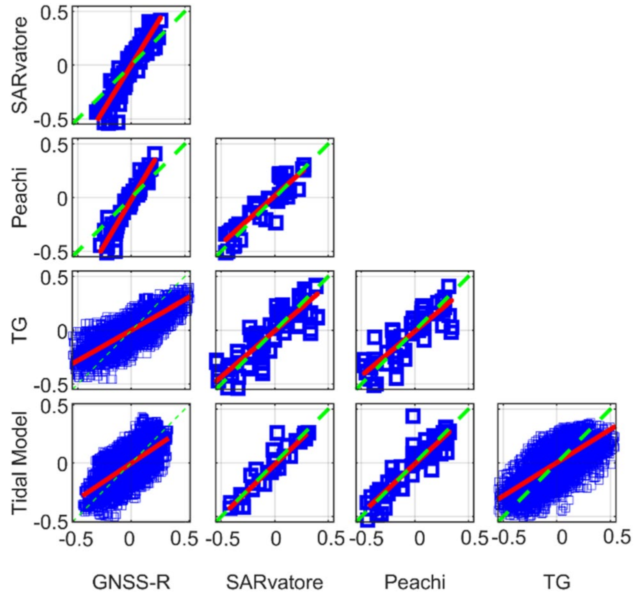

Fig. 5 Scatterplot between the different instruments involved in the study

Upon comparison to TG, we obtained a correlation coefficient (ρ) of 0.84 with a standard deviation of regression residuals (σ) of 7.8 cm for GNSS-R, $\rho = 0.86$ and $\sigma = 12.4$ cm for SARvatore, and $\rho = 0.85$ and $\sigma = 12.8$ cm for Peachi. The above suggests a better agreement for GNSS-R than for SAR-altimetry when each one is compared to the TG measurements. In comparison to the tidal model employed, the GNSS-R obtained a $\rho = 0.72$ and $\sigma = 9.8$ cm, indicating a slight degradation with respect to the GNSS-R vs. TG comparison. Moreover, we compared

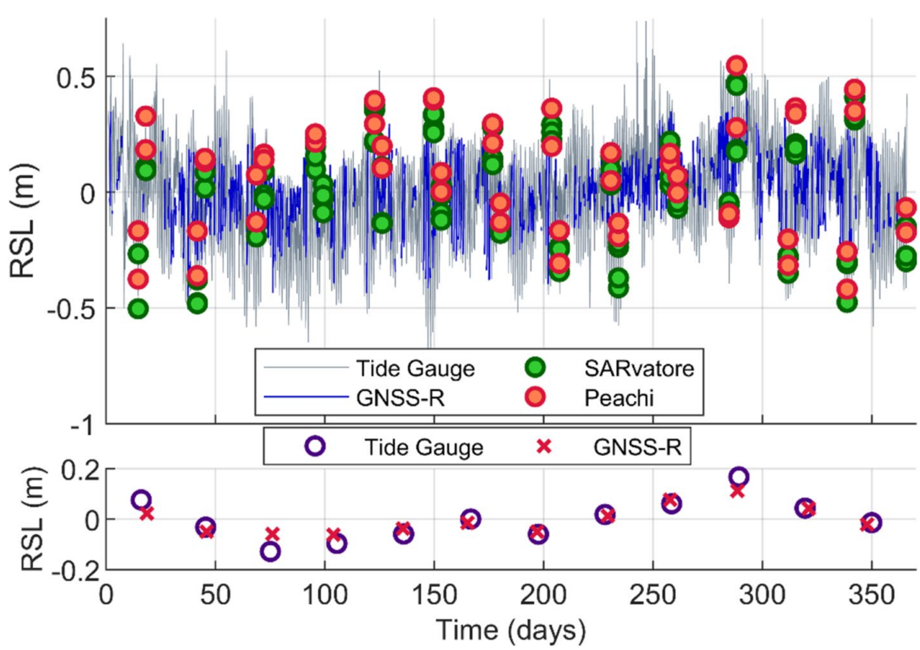

Fig. 4 Top panel presents the RSL retrievals during year 2017 from the GNSS-R tide gauge (blue line), Sentinel-3A SARvatore (green dot line), Sentinel-3A Peachi (orange dot line), and the conventional tide gauge (grey line). The bottom panel presents sea level monthly averages for the tide gauge and GNSS-R

Table 2 Statistics for the four analyzed techniques. The correlation coefficient (unitless), standard deviation of regression residuals (cm) and regression slope (m/m) are reported in this order for each combination

Instrument	GNSS-R	SARvatore	Peachi	Tide gauge
SARvatore	0.94/8.6/1.631			
Peachi	0.95/7.2/1.681	0.92/8.9/0.902		
Tide Gauge	0.84/7.8/0.554	0.86/12.4/0.843	0.85/12.8/0.814	
Tide Model	0.72/9.8/0.670	0.94/11.7/0.974	0.90/10.8/0.933	0.71/11.7/0.612

the GNSS-R and the two SAR-altimetry products, for which case it was obtained $\rho = 0.94$ and $\sigma = 8.6$ cm for SARvatore and $\rho = 0.95$ and $\sigma = 7.2$ cm for Peachi, indicating an improved agreement than in the two previous cases. Furthermore, the two SAR products had a correlation of 0.92 and a standard deviation of 8.9 cm, which can be interpreted as the noise floor of SAR altimetry at this location. Finally, we computed $\rho = 0.94$ and $\sigma = 1.9$ cm for monthly averages between the tide gauge and the GNSS-R, indicating a much better agreement in the lower frequency components.

It should be noted that the tide model performs better against SAR observations, because both are based on more open ocean sampling, where the sea level variations are more homogeneous. In contrast, the comparison of each coastal sensor (GNSS-R and TG) to the tide model is affected by higher spatial variability inherent in nearshore sea levels. It also is worth mentioning that the tidal model does not account for atmospheric phenomena, which further affects the comparisons.

In order to further assess the quality of the measurements, we applied a modified van de Casteele test (see Fig. 6). The shape and distribution of the points allow identifying numerous types of systematic errors in tide-gauge measurements (Miguez et al. 2008). For the case of SAR-altimetry, the data points are scattered on both sides of the diagram, suggesting that only random errors could be involved in the measurements. Based on Fig. 6, we confirm that the diagram presents an inclination, corroborating a scale error between GNSS-R and TG. This is in part due to the different tidal ranges present at the two separate locations. However, the scale error in GNSS-R compared to TG may also be partly attributable to land contamination. In this site with a small antenna height (1.8 m), FFZ at elevation angles greater than about 10° may cover both land and water. The situation is present even at high tides, although the effect is more pronounced at low tides when a larger area of the sand beach gets exposed to air. A proportional error arises, because the portion of FFZ covered by sand is greater at low tides and smaller at high tides. This effect causes an underestimation of the height of the antenna above the instantaneous surface in proportion to the height in question, which in its turn leads to an underestimation of tidal amplitude by GNSS-R.

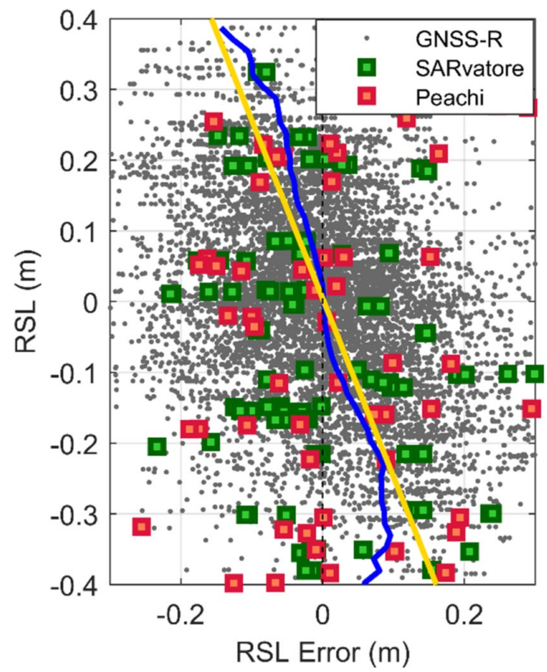

Fig. 6 Van de Casteele diagram for the GNSS-R and Sentinel-3A altimetry compared to the conventional tide gauge; GNSS-R smoothed error and regression is shown in blue curve and yellow line, respectively. The GNSS-R scale error attributed to land contamination is represented by the regression slope over the entire tidal range. The more pronounced GNSS-R anomaly at low tides arises at RSL $\lessapprox -0.2$ m

Furthermore, the instantaneous reflection footprint is not weighted homogeneously within and around each FFZ; rather, the reflection sensitivity kernel is skewed and decays gradually away from the specular point, with the near end of the FFZ contributing more to the formation of the reflection than the far end and beyond (Geremia-Nievinski et al. 2016). Thus, the exposed sandy beach tends to exert a strong influence on the partial sea surface reflection. In this sense, GNSS stations meant for coastal sea level measurements should be placed higher with respect to the reflective surface in order to avoid the land cover (Geremia-Nievinski and Hobiger 2019). In principle, using only data with lower elevation angle could avoid the aforementioned reflections, but this would lead to fewer GNSS-R observations, and the density of the time series would be reduced, making the GNSS-R solution unfeasible.

The online Supplementary Information presents results of the harmonic analysis performed and the comparison of amplitude and phase of the main tidal constituents across the two locations. K1 and O1 were found with major amplitude at the two sites. The centimetric amplitude difference found between the two locations is attributed to the ocean dynamics and sub-daily oscillations at the coast. Certainly, the FES2014b tidal model demonstrates the existence of variations in the tidal regime across the two sites in a smaller proportion. This key difference represents a good opportunity to assimilate GNSS-R data to improve modern tidal models further.

Conclusions

We have compared a coastal tide gauge (TG) and an insular GNSS reflectometry (GNSS-R) station to a tide model and two satellite products based on the Sentinel-3A synthetic aperture radar (SAR) altimetry mission. The inter-comparison was done to evaluate their consistency in measuring sea level variations over one year in the Gulf of Mexico, in a region composed of different conditions such as reefs, small islands, and shallow waters. The two remote sensing techniques performed reasonably well compared to the TG, obtaining a high correlation of 0.84 for GNSS-R and of 0.86 and 0.85 for SAR-altimetry. The GNSS-R and the tidal model had a correlation of 0.72, which may indicate effects absent from the tidal model. The correlation between GNSS-R and SAR was highest (0.94 and 0.95), better than that between TG and SAR (0.85), indicating that insular GNSS-R is a good opportunity to validate SAR measurements. The correlation between the two SAR technique products (0.92) represents the inherent uncertainty in SAR altimetry.

Furthermore, the comparison between TG and GNSS-R in terms of monthly averaged sea level yielded a correlation of 0.94 and σ of 1.9 cm, indicating good compatibility for long-term sea level change studies. On the other hand, we found systematic scale differences, as quantified by linear regression slope, which we attribute partially to the different tidal ranges experienced by each sensor and partially to land contamination in GNSS-R sea surface reflections when the sand beach gets exposed to air, especially during low tide. For the case of SAR-altimetry, more observations would be necessary in order to distinguish and identify its own specific systematic errors.

It is worth recognizing that the GNSS-R technique has worse precision than state-of-art TG, especially for raw or instantaneous sea surface height retrievals, making it more comparable to TG when forming daily averages. Therefore, the GNSS-R-based water level sensing cannot still replace a conventional TG in terms of precision, especially at high temporal resolution. We thus demonstrate that GNSS-R can act as a secondary data source, supplementing TG for long-term stability and as a good opportunity for spaceborne SAR altimetry validation in coastal and insular zones.

We also note each sea level sensor has its own strengths and weaknesses, so intercomparisons such as the present one serve for mutual validation and quality control. After the successful initial demonstration from this study, we recommend the processing of longer time series as future work. Multi-year series would allow separating seasonal effects from long-term trends in the assessment of contemporary sea level change in the Gulf of Mexico. Thus, the present technical contribution related to GNSS-R and other remote sensing techniques, paves the way for a future contribution related to geosciences and oceanography.

It should be noted that to consider the seasonal sea-level changes and long-term trends; it would require many years of data from tide gauge, GNSS-R and satellite altimetry for the same time span, which is very difficult to find at some places. Moreover, considering only one year of data, it would be affected by decadal effects such as El Niño or La Niña that could not be disentangled. Furthermore, according to Boretti (2019), in a longer-term analysis, it would be necessary to consider the vertical land motion using GNSS positioning since subsidence is the main contributor to sea-level rise in many areas of the world and the Mexican Caribbean it is not exempt. Therefore, these phenomena will be considered for future research.

Supplementary Information The online version contains supplementary material available at https://doi.org/10.1007/s10291-021-01207-x.

Acknowledgements The first author thanks the National Council for Science and Technology (CONACyT) of Mexico for granting a scholarship to accomplish this study (Grant #487690). We would like to thank the UNAVCO support team for the GPS data provided (UNAVCO Community 2016). The tide gauge station (Progreso) data is provided by the Intergovernmental Oceanographic Commission of UNESCO (IOC-UNESCO) at http://www.ioc-sealevelmonitoring.org. The Fresnel-zone map was developed using the software tools for GNSS interferometric reflectometry (Roesler and Larson 2018).

Funding The present work was supported by the National Council of Science and Technology (CONACyT-Mexico).

Data Availability The data used to support the findings are available from the corresponding author upon request. The Peachi altimetry data and FES2014b tidal model can be accessed from the AVISO + File Transfer Protocol (FTP) database service: ftp-access.aviso.altimetry.fr.

Declarations

Code availability The code used to compute FES2014 was developed in collaboration between Legos, Noveltis, CLS Space Oceanography Division and CNES which is available under GNU General Public License and can be freely accessed online at https://bitbucket.org/cnes_aviso/fes.

References

Aldarias A, Gomez-Enri J, Laiz I, Tejedor B, Vignudelli S, Cipollini P (2020) Validation of sentinel-3A SRAL coastal sea level data at high posting rate: 80 Hz. IEEE Trans Geosci Remote Sens 58(6):3809–3821. https://doi.org/10.1109/TGRS.2019.2957649

Anderson KD (2000) Determination of water level and tides using interferometric observations of GPS signals. J Atmos Ocean Technol 17(8):1118–1127. https://doi.org/10.1175/1520-0426(2000)017%3c1118:DOWLAT%3e2.0.CO;2

Axelrad P, Larson KM, Jones B (2005) Use of the correct satellite repeat period to characterize and reduce site-specific multipath errors. In: Proceedings of the 18th int tech meet satell div inst navig ION GNSS, 2638–2648 2005

Bilich A, Axelrad P, M. Larson K (2007) Scientific utility of the signal-to-noise ratio (SNR) reported by geodetic GPS receivers. In: Proceedings of the 20th int tech meet satell div inst navig ION GNSS, 1999–2010 2007

Birgiel E, Ellmann A, Delpeche-Ellmann N (2019) Performance of sentinel-3A SAR altimetry retrackers: the SAMOSA coastal sea surface heights for the baltic sea. In: Mertikas SP, Pail R (eds) Fiducial reference measurements for altimetry. Springer International Publishing, Cham, pp 23–32

Boretti A (2019) A realistic expectation of sea level rise in the Mexican Caribbean. J Ocean Eng Sci 4(4):379–386. https://doi.org/10.1016/j.joes.2019.06.003

Braun JJ, Mattioli GS, Calais E, Carlson D, Dixon TH, Jackson ME, Kursinski ER, Mora-Paez H, Miller MM, Pandya R, Robertson R, Wang G (2012) Focused study of interweaving hazards across the Caribbean. Eos Trans Am Geophys Union 93(9):89–90. https://doi.org/10.1029/2012EO090001

Cipollini P, Calafat FM, Jevrejeva S, Melet A, Prandi P (2017) Monitoring sea level in the coastal zone with satellite altimetry and tide gauges. Surv Geophys 38(1):33–57. https://doi.org/10.1007/s10712-016-9392-0

Cuevas-Jimenez A, Euan-Avila J (2009) Morphodynamics of carbonate beaches in the Yucatan Peninsula. Cienc Mar 35(3):307–320

Dinardo S (2013) Guidelines for the SAR (Delay-Doppler) L1b processing. ESA 3(2):20

Dinardo S, Fenoglio-Marc L, Buchhaupt C, Becker M, Scharroo R, Joana Fernandes M, Benveniste J (2018) Coastal SAR and PLRM altimetry in German Bight and West Baltic Sea. Adv Space Res 62(6):1371–1404. https://doi.org/10.1016/j.asr.2017.12.018

Geremia-Nievinski F, Hobiger T (2019) Site guidelines for multipurpose GNSS reflectometry stations. Zenodo. https://doi.org/10.5281/zenodo.3660744

Geremia-Nievinski F, Silva e MF, Boniface K, Monico JFG (2016) GPS diffractive reflectometry: footprint of a coherent radio reflection inferred from the sensitivity kernel of multipath SNR. IEEE J Sel Top Appl Earth Obs Remote Sens 9(10):4884–4891. https://doi.org/10.1109/JSTARS.2016.2579599

Geremia-Nievinski F, Hobiger T, Haas R, Liu W, Strandberg J, Tabibi S, Vey S, Wickert J, Williams S (2020a) SNR-based GNSS reflectometry for coastal sea-level altimetry: results from the first IAG inter-comparison campaign. J Geod 94(8):70. https://doi.org/10.1007/s00190-020-01387-3

Geremia-Nievinski F, Makrakis M, Tabibi S (2020b) Inventory of published GNSS-R stations, with focus on ocean as target and SNR as observable. Zenodo. https://doi.org/10.5281/zenodo.3660521

Holden LD, Larson KM (2021) Ten years of Lake Taupō surface height estimates using the GNSS interferometric reflectometry. J Geod 95(7):74. https://doi.org/10.1007/s00190-021-01523-7

Larson KM, Ray RD, Nievinski FG, Freymueller JT (2013) The accidental tide gauge: A GPS reflection case study from kachemak bay. Alaska IEEE Geosci Remote Sens Lett 10(5):1200–1204. https://doi.org/10.1109/LGRS.2012.2236075

Larson KM, Ray RD, Williams SDP (2017) A 10-year comparison of water levels measured with a geodetic GPS receiver versus a conventional tide gauge. J Atmos Ocean Technol 34(2):295–307. https://doi.org/10.1175/JTECH-D-16-0101.1

Löfgren JS, Haas R, Scherneck H-G (2014) Sea level time series and ocean tide analysis from multipath signals at five GPS sites in different parts of the world. J Geodyn 80:66–80. https://doi.org/10.1016/j.jog.2014.02.012

Lumban-Gaol J, Adrian D, Vignudelli S, RobertR L, Wayan Nurjaya I, Osawa T, Manurung P, Arhatin RE (2018) An assessment of a coastal altimetry data product in the Indonesian Waters. IOP Conf Ser Earth Environ Sci 176:012034. https://doi.org/10.1088/1755-1315/176/1/012034

Martin-Neira M (1993) A passive reflectometry and interferometry system (PARIS): application to ocean altimetry. ESA J 17(4):331–355

Miguez BM, Testut L, Wöppelmann G (2008) The van de casteele test revisited: an efficient approach to tide gauge error characterization. J Atmos Ocean Technol 25(7):1238–1244. https://doi.org/10.1175/2007JTECHO554.1

Nievinski FG, Larson KM (2014a) Inverse modeling of GPS multipath for snow depth estimation—part I: formulation and simulations. IEEE Trans Geosci Remote Sens 52(10):6555–6563. https://doi.org/10.1109/TGRS.2013.2297681

Nievinski FG, Larson KM (2014b) Inverse modeling of GPS multipath for snow depth estimation—part II: application and validation. IEEE Trans Geosci Remote Sens 52(10):6564–6573. https://doi.org/10.1109/TGRS.2013.2297688

Ray C, Martin-Puig C, Clarizia MP, Ruffini G, Dinardo S, Gommenginger C, Benveniste J (2015) SAR altimeter backscattered waveform model. IEEE Trans Geosci Remote Sens 53(2):911–919. https://doi.org/10.1109/TGRS.2014.2330423

Roesler C, Larson KM (2018) Software tools for GNSS interferometric reflectometry (GNSS-IR). GPS Solut 22(3):80. https://doi.org/10.1007/s10291-018-0744-8

Soulat F, Caparrini M, Germain O, Lopez-Dekker P, Taani M, Ruffini G (2004) Sea state monitoring using coastal GNSS-R: sea state monitoring using GNSS-R. Geophys Res Lett. https://doi.org/10.1029/2004GL020680

Tabibi S, Geremia-Nievinski F, van Dam T (2017) Statistical comparison and combination of GPS, GLONASS, and multi-GNSS multipath reflectometry applied to snow depth retrieval. IEEE Trans Geosci Remote Sens 55(7):3773–3785. https://doi.org/10.1109/TGRS.2017.2679899

Tabibi S, Geremia-Nievinski F, Francis O, van Dam T (2020) Tidal analysis of GNSS reflectometry applied for coastal sea level sensing in Antarctica and Greenland. Remote Sens Environ 248:111959.https://doi.org/10.1016/j.rse.2020.111959

Valladeau G, Thibaut P, Picard B, Poisson JC, Tran N, Picot N, Guillot A (2015) Using SARAL/AltiKa to improve Ka-band altimeter measurements for coastal zones, hydrology and ice: the peachi prototype. Mar Geod 38(sup1):124–142. https://doi.org/10.1080/01490419.2015.1020176

UNAVCO Community (2016) COCONet GPS Network - CN26-ArrecifeAMEX2016 P.S. GAGE Facil Oper UNAVCO Inc GNSS Obs Dataset. https://doi.org/10.7283/W1SE-3691

Publisher's Note Springer Nature remains neutral with regard to jurisdictional claims in published maps and institutional affiliations.

Carlos A. Martinez-Felix received the B.E. degree in Mechatronics from Instituto Tecnológico de Culiacán, México in 2012, and M.S. degree in Information Science from Universidad Autónoma de Sinaloa, México in 2017. He is currently working toward the Ph.D. degree at the Department of Earth and Space Science, UAS, Mexico. His research interests include the remote sensing of the environment using GNSS Multipath Reflectometry.

G. Esteban Vazquez-Becerra is a professor at the Department of Earth and Space Sciences, Autonomous University of Sinaloa, Mexico. He received his M.S. and Ph.D. in Geodesy from the Department of Civil and Environmental Engineering and Geodetic Science at Ohio State University in 2002 and 2009. His research interest covers GPS atmospheric research and precise DGPS static positioning and deformations.

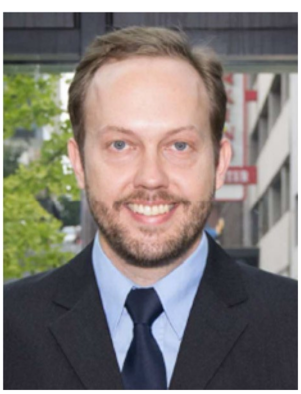

Felipe Geremia-Nievinski Received the B.E. degree in geomatics from Universidade Federal do Rio Grande do Sul (UFRGS), Porto Alegre-RS, Brazil, in 2005, the M.Sc.E. degree in geodesy from the University of New Brunswick, Fredericton, NB, Canada, in 2009, and the Ph.D. degree in aerospace engineering sciences from the University of Colorado Boulder, Boulder, CO, USA, in 2013.

Jesus R. Millan-Almaraz received an M.E. degree in electrical engineering from the University of Guanajuato, Mexico, in 2008 and a Ph.D. from the Autonomous University of Queretaro, Mexico. He is currently working at the Physics and Mathematics Faculty, Autonomous University of Sinaloa, Mexico. His research interests include digital signal processing, instrumentation, and embedded systems.

Cuauhtemoc Franco-Ochoa received his M.S. and Ph.D. in Construction and Hydraulic Engineering from the National Autonomous University of Mexico. He is an Assistant Professor in the Civil Engineering Department at the Autonomous University of Sinaloa in Mexico with research interests in coastal and rivers morphodynamics, and numerical modeling of coastal processes.

Angela Melgarejo-Morales received an M.S. degree in Information Science from the Universidad Autónoma de Sinaloa (UAS), Culiacan, Mexico in 2017. She is currently a Ph.D. student at the Department of Earth and Space Science at UAS with research interests in ionospheric anomalies via GPS data and its correlation with earthquake forecasting.

J. Ramon Gaxiola-Camacho received his M.S. and Ph.D. in Civil Engineering and Engineering Mechanics from the University of Arizona in 2015 and 2017, respectively. Since June 2017, he is an Assistant Professor in the Civil Engineering Department at the Autonomous University of Sinaloa in Mexico. His research topics are related to reliability analysis, probabilistic methods and health assessment of infrastructure.